Journal of Materials Chemistry C

ROYAL SOCIETY OF CHEMISTRY

PAPER

View Article Online
View Journal | View Issue

Cite this: J. Mater. Chem. C, 2020, 8, 8091

Negative-pressure enhanced ferroelectricity and piezoelectricity in lead-free $BaTiO_3$ ferroelectric nanocomposite films†

Xiyuan Zhang,[a] Ruixing Xu,[a] Xingyao Gao,[b] Yanda Ji,[a] Fengjiao Qian,[a] Jiyu Fan,*[a] Haiyan Wang,[b] Weiwei Li*[c] and Hao Yang*[ad]

Received 26th March 2020,
Accepted 18th May 2020

DOI: 10.1039/d0tc01556c

rsc.li/materials-c

Due to environmental concerns and the increasing drive towards miniaturization of electronic circuits and devices, lead-free ferroelectric films with low leakage current and robust ferroelectric and piezoelectric properties are highly desired. The preferred alternative, $BaTiO_3$, is non-toxic and has ferroelectric properties, but its high leakage current, poor ferroelectricity and piezoelectricity and low Curie temperature of ~130 °C in thin film form are obstacles for high-temperature practical applications. Here, we report that a negative-pressure-driven enhancement of ferroelectric Curie temperature and effective piezoelectric coefficient are achieved in (111)-oriented $BaTiO_3$ nanocomposite films. The enhanced ferroelectric and piezoelectric properties in the emergent monoclinic $BaTiO_3$ are attributed to the sharp vertical interface and 3D tensile strain that develops upon interspersing stiff and self-assembled vertical Sm_2O_3 nanopillars through the film thickness. Our work also demonstrates that fabricating oxide films through (111)-oriented epitaxy opens up new avenues for the creation of new phase components and exploration of novel functionalities for developing oxide quantum electronic devices.

1. Introduction

Ferroelectrics possess polarization that is spontaneous, stable and electrically switchable.[1] Due to the strong coupling between their electrical, mechanical, thermal, and optical responses, ferroelectrics have been widely investigated for a diverse range of applications such as non-volatile memory devices, sensing, capacitors, non-linear optical components, piezoelectric actuators, energy harvesting and storage, micro-electromechanical systems, and high-power electronic transducers.[2–6] Over the past few decades, industry-standard ferroelectric materials have been based on $Pb_{1-x}Zr_xTiO_3$ and contain lead, which is toxic and environmentally unfriendly.[7] In consideration of the growing demand for green materials with minimal impacts on health and environment, lead-free alternative materials are urgently needed.[8,9] Further, with the increasing drive towards miniaturization of electronic circuits and devices, stable piezoelectrics and ferroelectrics with a high Curie temperature and a low leakage current in film form are highly required. The preferred alternative, $BaTiO_3$, is non-toxic and has ferroelectric properties, but its high leakage current, poor piezoelectricity and ferroelectricity and a low Curie temperature of ~130 °C in thin film form limit high-temperature practical application in electronic devices.[10,11] Biaxial strain has been used to enhance the Curie temperature of epitaxial $BaTiO_3$ films, but only for thicknesses of tens of nanometers,[12] which is not thick enough for some device applications. Also, a high leakage current and a large coercive field reported in plain $BaTiO_3$ films pose significant challenges for achieving low-voltage operation and low power consumption in electronic devices.[13–17]

Benefiting from the advantages of substrate preparation techniques,[18] an interesting proposition is to rely on higher index surfaces such as (111).[19] Since its structure resembles a buckled honeycomb lattice similar to two-dimensional (2D) materials, the symmetry and interactions across epitaxial (111) interfaces have led to novel phenomena such as a polar metal phase in $NdNiO_3$ films,[20] exchange bias in $LaNiO_3$–$LaMnO_3$ superlattices,[21] and two-dimensional topological insulators.[22] Note that different crystallographic orientations can give rise to diverse interfacial coupling and resulting properties. For ferroelectric thin films, theoretical studies of in-plane strain applied along the (111) plane have predicted that the spontaneous polarization and Curie temperature of $BaTiO_3$ are insensitive to compressive strain,

[a] College of Science, Nanjing University of Aeronautics and Astronautics, Nanjing 211106, P. R. China. E-mail: jiyufan@nuaa.edu.cn, yanghao@nuaa.edu.cn
[b] School of Materials Engineering, Purdue University, West Lafayette, IN 47907, USA
[c] Department of Materials Science & Metallurgy, University of Cambridge, 27 Charles Babbage Road, Cambridge, CB3 0FS, UK. E-mail: wl337@cam.ac.uk
[d] Key Laboratory for Intelligent Nano Materials and Devices of the Ministry of Education, Nanjing University of Aeronautics and Astronautics, Nanjing 211106, P. R. China

† Electronic supplementary information (ESI) available. See DOI: 10.1039/d0tc01556c

but can be significantly enhanced by tensile strain (>2.5%).[23–25] However, there are very few experimental results because very limited commercial (111)-oriented substrates can be used for imposing such large tensile strain. Furthermore, similar to the well-studied (001)-oriented ferroelectric films, the in-plane (111) strain can only be maintained for thicknesses of tens of nanometers, which are not robust enough for many applications.

Recently, density-functional theory calculations predicted the enhanced ferroelectric properties of $PbTiO_3$ and $BaTiO_3$ ferroelectrics under negative pressure (or hydrostatic tensile stress).[26] By using the difference in the density of $PbTiO_3$ in the different phases, Wang *et al.* reported the negative-pressure-driven enhancement of ferroelectric and piezoelectric properties in free-standing $PbTiO_3$ and $Pb(Zr,Ti)O_3$ nanowires.[27,28]

Nevertheless, the effects of negative pressure associated with ferroelectric films grown along the (111) direction with hexagonal symmetry have received less attention. This is because horizontal strain engineering of ferroelectric thin films in layered heterostructures is incapable of expansion in three mutually perpendicular directions, that is, negative pressure. A novel method to achieve negative pressure control in much thicker films involves the growth of self-assembled vertical nanocompsosites.[29–32] In $YBa_2Cu_3O_{7-\delta}$:$BaZrO_3$ nanocomposite films, in-plane and out-of-plane lattice expansion (or negative pressure) have been demonstrated in the $YBa_2Cu_3O_{7-\delta}$ phase, with a strong modification of superconductive properties.[31,33]

Here, we report the nanocomposite films of $BaTiO_3$:Sm_2O_3 grown on (111)-oriented 0.5 wt% Nb-doped $SrTiO_3$ substrates that generate negative pressure in $BaTiO_3$. It was found that rare earth elements may diffuse in ferroelectrics.[34,35] Sm_2O_3 was selected as the second phase for strain control because it has been confirmed that it substitutes very minimally into $BaTiO_3$.[14] Besides, Sm_2O_3 has a large elastic modulus of 125 GPa, compared to 67 GPa for $BaTiO_3$, and it is very insulating.[32,36,37] In 500 nm-thick films, we demonstrate the negative-pressure-driven enhancement of the ferroelectric Curie temperature, from 130 °C to 616 °C, and a large longitudinal effective piezoelectric coefficient d_{33}^{eff} ($\sim$80 pm V^{-1}) in the emergent monoclinic $BaTiO_3$. Such enhancements of ferroelectric and piezoelectric properties in thick films open up new avenues to use $BaTiO_3$ in high-temperature ferroelectric film applications.

2. Experimental details

Pulsed laser deposition was used to grow high-quality plain $BaTiO_3$ and $(BaTiO_3)_{0.5}$:$(Sm_2O_3)_{0.5}$ nanocomposite films on (111)-oriented 0.5 wt% Nb-doped $SrTiO_3$ substrates. The growth temperatures were optimized at 800 °C, with an oxygen partial pressure of 0.25 mbar, with a laser fluence of 1–2 J cm^{-2}, and at a laser repetition rate of 2–4 Hz. The distance between target and substrate was set to 8 cm. All films were cooled at a rate of 5 °C min^{-1} to ambient temperature in a static-oxygen pressure of 0.8 atm. High-resolution four circle X-ray diffraction (PANalytical Empyrean, Kα radiation) and scanning transmission electron microscopy (STEM, FEI Tecnai F20 analytical microscope) were used to investigate the crystallography of the thin films.

Top Au electrodes with an area of 3.14×10^{-4} cm^2 were sputtered for the dielectric measurements. Dielectric permittivity was calculated from the measured capacitance (C) using $C = \varepsilon_0\varepsilon_r A/d$, where A is the area of the top electrode and d is the thickness of the film. The dielectric measurements were carried out using an Impedance Analyzer (E4990A). For the ferroelectric measurements, the top Au electrodes with an area of 7.85×10^{-5} cm^2 were deposited by sputtering. Ferroelectric hysteresis loops were measured using a Radiant Precision materials analyzer. The temperature was controlled by using a Linkam Scientific Instruments HFS600E-PB4 system. Piezoresponse force microscopy measurements were conducted using an Asylum Research AFM MFP-3D origin with an Environmental Controller and a HVA220 High Voltage Amplifier. The Environment Controller, HVA220 High Voltage Amplifier and the ARC2 Controller were connected in series, and the sample was placed on the variable temperature holder. The temperature can be raised to the target temperature and the maximum temperature for the stability test was 200 °C.

3. Results and discussion

Fig. 1a shows the X-ray diffraction (XRD) θ–2θ scans of the plain $BaTiO_3$ film and $BaTiO_3$:Sm_2O_3 nanocomposite film, revealing that all films are epitaxial and contain no intermixed crystalline phases. Compared to the plain $BaTiO_3$ film, the $BaTiO_3$ peak for the nanocomposite film shifts towards a lower angle, indicating an increase of the out-of-plane lattice parameter. To minimize the out-of-plane lattice mismatch and interfacial energy with (111) Nb:STO, $BaTiO_3$ and Sm_2O_3 exhibit (111) and (224) orientations in the nanocomposite films, respectively. This result is confirmed by a selected area diffraction (SAD) image, which also reveals the in-plane orientations for $(110)_{BTO}\|(110)_{STO}\|(004)_{Sm_2O_3}$ and $(001)_{BTO}\|(001)_{STO}\|(220)_{Sm_2O_3}$ (Fig. S1, ESI†). From scanning transmission electron microscopy (STEM) images (Fig. 1b and Fig. S1, ESI†), we can see that self-assembled Sm_2O_3 nanopillars are distributed and embedded in a $BaTiO_3$ matrix. Also, an interface without visible misfit dislocation is formed along the interface between $BaTiO_3$ and Sm_2O_3 (Fig. S1, ESI†). To examine the change of lattice parameters for the (111) oriented films, X-ray reciprocal space map (RSM) studies were performed and the results are shown in Fig. 1c. From a combination of θ–2θ scans and RSMs, the lattice parameters of a, b, and c were calculated and are presented in Table 1. In the plain $BaTiO_3$ film, the in-plane lattice parameters are similar to those of the $BaTiO_3$ bulk and the out-of-plane lattice parameter is slightly larger than that of the $BaTiO_3$ bulk.[38] This indicates that stoichiometric $BaTiO_3$ films were fabricated. It was reported that an increase of the out-of-plane lattice parameter can be induced by an increase of out-of-plane domains when the $BaTiO_3$ film domain pattern gets more distorted.[39] The tilted lattices and nanodomains can be further formed by ferroelectric distortion. As a consequence, the lattice parameters can be increased through the phase transition.[40] In the $BaTiO_3$:Sm_2O_3 nanocomposite film, due to the stiff Sm_2O_3 nanopillars with diameters of 3–5 nm embedded in the $BaTiO_3$ matrix, we found that the lattice constants of a, b, and c in $BaTiO_3$ are increased (Table 1), indicating

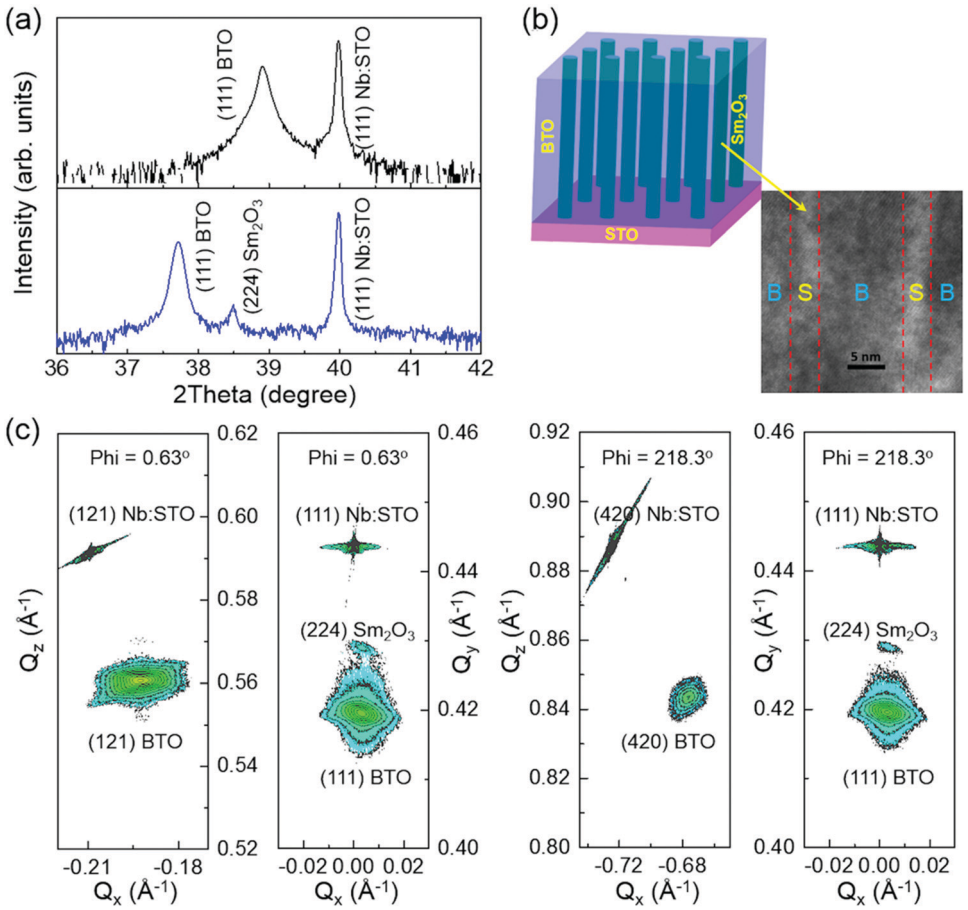

Fig. 1 (a) XRD θ–2θ scans for plain $BaTiO_3$ 100 nm film and $BaTiO_3$:Sm_2O_3 500 nm nanocomposite film grown on (111) Nb:$SrTiO_3$. (b) Top panel: A schematic diagram of the VAN structure. Bottom panel: Cross-sectional STEM image of BTO:Sm_2O_3 film. B is BTO and S is Sm_2O_3. (c) X-ray reciprocal space maps (RSMs) of the (121), (420), and (111) Bragg reflections of Nb:$SrTiO_3$, $BaTiO_3$, and Sm_2O_3 at Phi = 0.63° and Phi = 218.3° for calculating the lattice parameters and lattice angles of $BaTiO_3$ in the 500 nm-thick nanocomposite film. Phi is an azimuth angle of the nanocomposite film for achieving specific Bragg reflections in RSM measurements.

Table 1 Lattice parameters and angles of $BaTiO_3$ in bulk and thin films

	Lattice parameter (Å, a)	Lattice parameter (Å, b)	Lattice parameter (Å, c)	Lattice angles (°)
$BaTiO_3$ bulk[38]	3.9938	3.9938	4.0361	$\alpha, \beta, \gamma = 90$
Plain $BaTiO_3$ 100 nm	3.995 ± 0.008	3.994 ± 0.006	4.065 ± 0.007	$\alpha, \beta, \gamma = 90$
$BaTiO_3$ in 500 nm nanocomposite film	4.151 ± 0.005	4.135 ± 0.005	4.122 ± 0.007	$\alpha, \gamma = 90$ $\beta = 99.01$

that negative pressure is formed in the nanocomposite films. The lattice angles of α, β, and γ were further calculated by $\cos\theta = \frac{\vec{a}\cdot\vec{b}}{|a||b|}$, yielding $\alpha = \gamma = 90^\circ$ and $\beta = 99.01^\circ$ for $BaTiO_3$ in the nanocomposite films (Table 1). Together with the observation of lattice parameters that $a \neq b \neq c$, it was revealed that $BaTiO_3$ has a monoclinic structure (Fig. S2, ESI†), consistent with the tensile strain-driven monoclinic structure predicted by the density-functional theory calculation.[23–26]

To explore the negative pressure effect on the Curie temperature of $BaTiO_3$, temperature-dependent XRD results are presented in Fig. 2a and Fig. S4 (ESI†). The temperature-dependent evolution of the lattice parameter d_{222} reveals two regimes over the temperature range from 25 to 900 °C separated by a kink that is characteristic of a phase transition. The presence of phase transitions at ~180 °C, ~368 °C, and ~616 °C for the plain $BaTiO_3$ film, and 100 nm and 500 nm nanocomposite films, respectively, was observed. For the plain $BaTiO_3$ film, the transition is close to that of the $BaTiO_3$ bulk (~130 °C).[11] However, for the 500 nm-thick nanocomposite film, the phase transition is significantly enhanced to ~616 °C. To verify the phase transitions observed in the XRD studies, we probed the temperature dependence of the dielectric permittivity (Fig. 2b). For the plain $BaTiO_3$ film, a broad peak is observed and the Curie temperature is determined to be ~160 °C. This value is similar to that of the plain (001)-oriented $BaTiO_3$ film reported in the literature.[14,41,42] For the 500 nm-thick

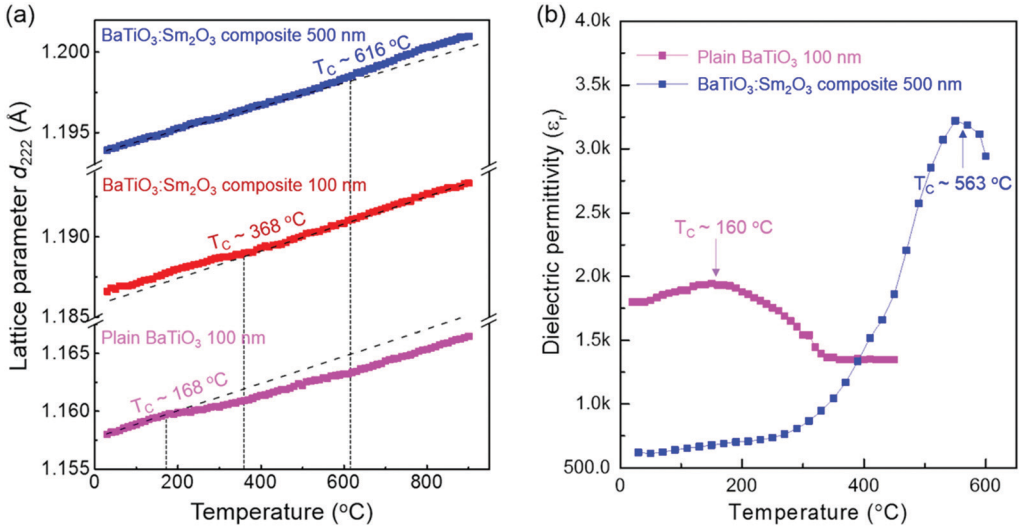

Fig. 2 (a) Temperature dependent lattice parameter d_{222} of plain $BaTiO_3$ film and $BaTiO_3$:Sm_2O_3 nanocomposite films. Two distinct regimes separated by a kink in the lattice parameter are observed. (b) Dielectric permittivity of plain $BaTiO_3$ film and $BaTiO_3$:Sm_2O_3 nanocomposite film measured as a function of temperature at 50 kHz.

nanocomposite film, we observed that the Curie temperature is ~563 °C. This value is in agreement with the phase transition measured from the XRD studies and confirms the presence of a ferroelectric-to-paraelectric phase transition at this temperature. We conclude that, due to the negative pressure, the Curie temperature of $BaTiO_3$ is strongly enhanced from ~130 °C to ~616 °C in the 500 nm-thick nanocomposite film.

From ferroelectric hysteresis measurements, the 500 nm-thick nanocomposite film was confirmed to be ferroelectric up to at least 300 °C (Fig. 3a). A robust remanent polarization (P_r) of 23 μC cm^{-1}, which was calculated using the area of the BTO component in the nanocomposite film, was recorded both at room temperature and 300 °C. The room temperature value is significantly higher than that of the plain $BaTiO_3$ film (Fig. S5, ESI†), and similar to that of the (001)-oriented $BaTiO_3$ films from the literature.[14,16,17,43] The high piezoelectricity found in $PbZr_{1-x}Ti_xO_3$ and related $PbTiO_3$ solid solution materials originates from the presence of a monoclinic crystal structure and the formation of nanodomains at the morphotropic phase boundary (MPB).[44–46] Thus, ferroelastic nanodomain structures and low-symmetry monoclinic phases are helpful for inducing large piezoelectricity. In ferroelectric films, epitaxial strain also offers the possibility to enhance the effective piezoelectric properties (d_{33}^{eff}) utilizing low crystal symmetries and a high density of domain walls.[39] Note that reducing the domain size can improve the effective piezoelectric properties (d_{33}^{eff}) in the (111)-oriented $BaTiO_3$ single crystals.[47] Piezoresponse force microscopy (PFM) was further applied to explore the piezoelectricity in the 500 nm-thick nanocomposite film. Although it is a daunting challenge to accurately measure the effective piezoelectric coefficient (d_{33}^{eff})

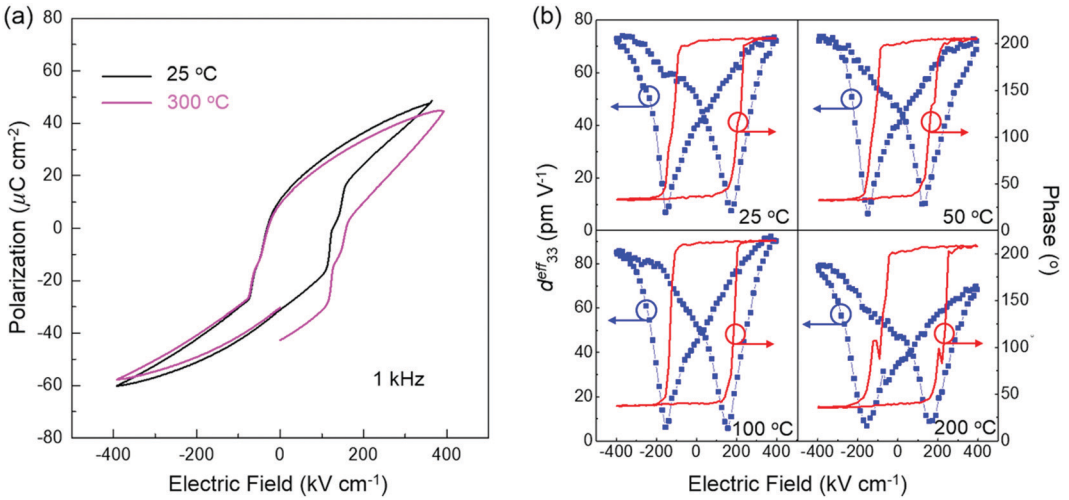

Fig. 3 (a) Ferroelectric hysteresis loops of 500 nm-thick $BaTiO_3$:Sm_2O_3 nanocomposite film at 25 °C and 300 °C revealing the presence of strong and robust polarization even at 300 °C. (b) Effective piezoelectric coefficient d_{33}^{eff} and phase hysteresis loops of 500 nm-thick $BaTiO_3$:Sm_2O_3 nanocomposite film measured from 25 °C to 200 °C.

through PFM, several works have reported the measurement of effective values for d_{33}^{eff}.[48–50] Meanwhile, some other evidence has been sought to demonstrate the inherent difficulties associated with quantitative d_{33}^{eff}.[51–55] As discussed in the literature studies, the selection of the cantilever, the uncertainty of the contact between the tip coating and tip surface and electrostatic effects all lead to a decrease of the credibility of PFM as a quantitative tool. Considering these factors, some preventive measures were first taken to minimize the negative impact. Measurements were carried out on the same position of the same sample with the same cantilever and at the same laser spot position on the cantilever backside, which are known to affect the results. Electrostatic effects were ignored due to the relatively stiff cantilever used (1.4–5.8 N m^{-1}) and the grounding of samples. To obtain the deformation of the piezoelectric material due to the application of the voltage, switching spectroscopy PFM (SS-PFM) was conducted to obtain the measured piezoresponse amplitude as a function of driving frequency, f,

$$A(f) = \frac{f_0^2 A_d}{\sqrt{(f_0^2 - f^2)^2 + \left(\frac{f_0 f}{Q}\right)^2}}. \quad (1)$$

where A_d is the amplitude of the electric-field-induced deformation driving the system, Q is the quality factor and f_0 is the resonant frequency. In addition, SS-PFM measurements were performed in dual AC resonance tracking (DART) mode, which used two excitation frequencies f_1, f_2 and led to four measured quantities, namely the corresponding amplitudes A_1, A_2 and phases Φ_1, Φ_2. As a result, A_d can be calculated from the obtained values of Q and f_0.[56] The effective piezoelectric coefficient d_{33}^{eff} was extracted from $A_d = (d_{33}^{eff})V_{ac}$, where V_{ac} is the drive amplitude. Besides, it is worth noting that, in the conventional approach, PFM amplitude and phase are acquired at a fixed frequency, which are insufficient for the determination of the full characteristics of the tip–surface junction in the framework of a simple harmonic oscillator (SHO) model.[53,54] A SHO model is characterized by resonance frequency, whose amplitude and phase at the resonance frequency and Q-factor are independent. But, in single-frequency PFM, only two independent parameters, *i.e.*, the amplitude and phase, are measured at a fixed frequency, and therefore, they are inadequate to describe the system completely. In this work, multiple frequencies are selected to determine the SHO model parameters for the tip–surface junction. The response is measured over the same band of frequency and Fourier transformed to get the amplitude and phase as a function of frequency. However, this approach will inevitably enhance the piezoelectric response by increasing the signal-to-noise ratio due to resonance. As shown in Fig. S6 (ESI†), SHO fitting was used to reduce the increase in signal-to-noise ratio caused by the resonance and quantify the accurate A_d.

With the limitation of the instrument (PFM sample heater) and stability of the PFM cantilevers used, robust butterfly loops of piezeoelectricity and phase hysteresis loops were obtained with PFM spectroscopic measurements from room temperature to 200 °C (Fig. 3b). As discussed above, although it is still very difficult to quantify d_{33} by PFM, a non-decreasing effective piezoelectric coefficient (d_{33}^{eff}) with a value of ~80 pm V^{-1} was measured from room temperature to 200 °C, indicating strong and stable piezoelectricity in $BaTiO_3$:Sm_2O_3 nanocomposite films. Meanwhile, the value (~80 pm V^{-1}) is the highest effective piezoelectric coefficient ever recorded compared with that of $BaTiO_3$ films measured using PFM.[57–59] Also, compared to the (111)-oriented plain $BaTiO_3$ films,[60,61] our (111)-oriented

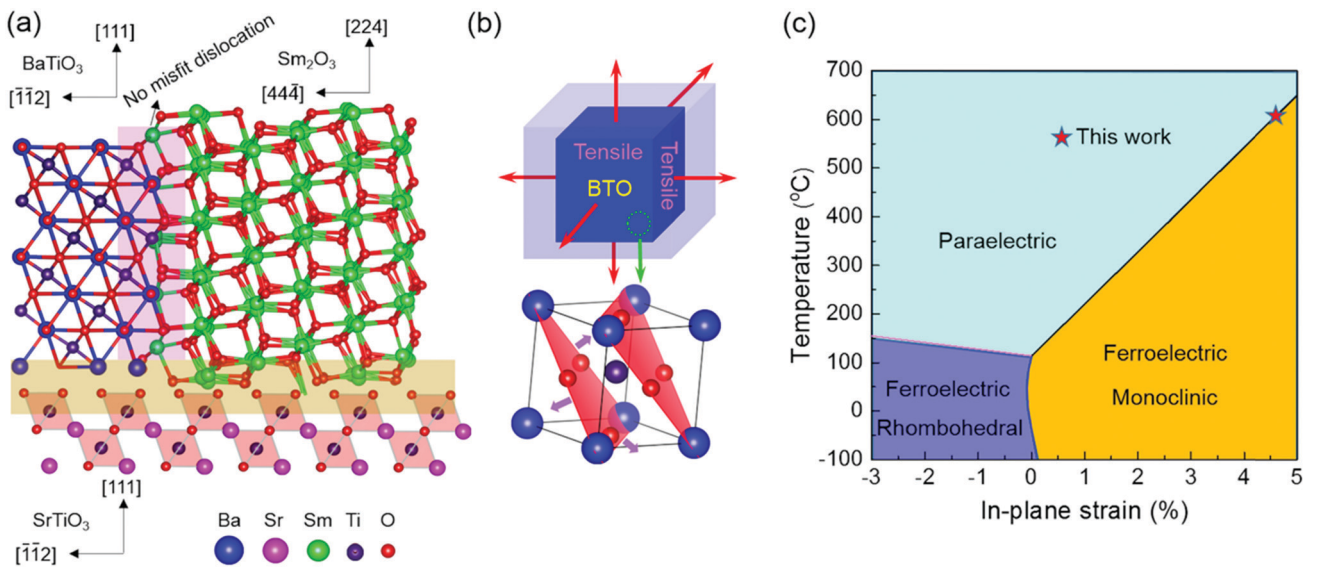

Fig. 4 (a) Crystallographic model of the $BaTiO_3$:Sm_2O_3 nanocomposite film around the vertical interface between $BaTiO_3$ and Sm_2O_3. (b) Schematic diagram of 3D tensile strain applied to $BaTiO_3$. The thin arrows in the top panel represent the tensile strain applied along the three mutually perpendicular directions. The thick arrows in the bottom panel represent the three oxygen atoms around the Ti atom that move away from each other after applying 3D tensile strain. (c) Temperature-dependent in-plane strain phase diagram of (111)-oriented $BaTiO_3$ from theoretical calculation.[24] The star represents the ferroelectric Curie temperature of $BaTiO_3$ in the 500 nm-thick nanocomposite film.

$BaTiO_3$:Sm_2O_3 nanocomposite films have the largest effective piezoelectric coefficient and a relatively high ferroelectric Curie temperature.

Based on the above mentioned discussion and results, a crystallographic model of the vertical interface between $BaTiO_3$ and Sm_2O_3 is presented in Fig. 4a. Due to the negative pressure (or 3D tensile strain) applied along the three mutually perpendicular directions (Fig. 4b), in this case, the three oxygen atoms around the Ti atom move away from each other and create an empty space at the center of the oxygen triangle, which allows the Ti atom to move off-center, which can significantly enhance the ferroelectric Curie temperature. This is consistent with (111) $BaTiO_3$:Sm_2O_3 nanocomposite films, compared to the plain (111) $BaTiO_3$ films. Fig. 4c shows the theoretical calculation of the in-plane strain phase diagram for (111)-oriented $BaTiO_3$.[24] We can see that the ferroelectric Curie temperature is enhanced by the tensile strain and the monoclinic phase is also stabilized under the tensile strain.[24,62] In addition, the enhanced ferroelectric Curie temperature of (111)-oriented $BaTiO_3$ in nanocomposite films is equivalent to that of plain (111)-oriented $BaTiO_3$ films subjected to an in-plane strain value of $\sim$4.5%, which was impossible to achieve in the plain films.

4. Conclusions

In summary, strongly enhanced ferroelectricity and piezoelectricity were achieved in self-assembled nanocomposite films of $BaTiO_3$ and Sm_2O_3. The strong and robust remanent polarization and effective piezoelectric coefficient can be maintained up to at least 300 °C and 200 °C, respectively. The enhancement of ferroelectric Curie temperature ($\sim$616 °C) and effective piezoelectric coefficient ($\sim$80 pm V^{-1}) is attributed to the negative pressure generated by strain coupling between stiff Sm_2O_3 nanopillars and the surrounding $BaTiO_3$ matrix. Through the (111)-oriented epitaxial films, our results demonstrate a new promising route to creating negative pressure and developing lead-free ferroelectric films with the formation of new phase components that improve their Curie temperature and exploitable properties for applications. The enhanced ferroelectric and piezoelectric properties of $BaTiO_3$ may also enable the development of energy efficient quantum electronic devices.

Author contribution

H. Y. and W.-W. L. supervised the project. X. Z. fabricated the samples and carried out XRD, AFM, piezoelectric and ferroelectric measurements with the support from R. X., Y. J., F. Q. and J. F. X. G. and H. W. performed the STEM measurements. X. Z., W.-W. L. and H. Y. prepared the manuscript with contributions from all authors.

Conflicts of interest

There are no conflicts to declare.

Acknowledgements

This work was supported by the National Nature Science Foundation of China (Grant No. U1632122, 11774172 and 51602152), the Postgraduate Research & Practice Innovation Program of Jiangsu Province (KYCX18_0243) and the Open Fund of Key Laboratory for Intelligent Nano Materials and Devices of the Ministry of Education INMD-2019M06. X. G. and H. W. acknowledge the support from the U. S. National Science Foundation for the TEM analysis (DMR-1565822).

References

1 M. Dawber, K. M. Rabe and J. F. Scott, *Rev. Mod. Phys.*, 2005, **77**, 1083.
2 G. H. Haertling, *J. Am. Ceram. Soc.*, 1999, **82**, 797–818.
3 N. Setter, D. Damjanovic, L. Eng, G. Fox, S. Gevorgian, S. Hong, A. Kingon, H. Kohlstedt, N. Y. Park, G. B. Stephenson, I. Stolitchnov, A. K. Taganstev, D. V. Taylor, T. Yamada and S. Streiffer, *J. Appl. Phys.*, 2006, **100**, 051606.
4 G. Catalan and J. F. Scott, *Adv. Mater.*, 2009, **21**, 2463.
5 J. F. Scott, *Science*, 2007, **315**, 954–959.
6 Y.-M. You, W.-Q. Liao, D. Zhao, H.-Y. Ye, Y. Zhang, Q. Zhou, X. Niu, J. Wang, P.-F. Li, D.-W. Fu, Z. Wang, S. Gao, K. Yang, J.-M. Liu, J. Li, Y. Yan and R.-G. Xiong, *Science*, 2017, **357**, 306–309.
7 M. D. Maeder, D. Damjanovic and N. Setter, *J. Electroceram.*, 2004, **13**, 385–392.
8 E. Cross, *Nature*, 2004, **432**, 24.
9 D. Damjanovic, N. Klein, J. Li and V. Porokhinskyy, *Funct. Mater. Lett.*, 2010, **3**, 5.
10 T. Takenaka and H. Nagata, *J. Eur. Ceram. Soc.*, 2005, **25**, 2693.
11 M. Zgonik, P. Bernasconi, M. Duelli, R. Schlesser, P. Günter, M. H. Garrett and D. Rytz, *Phys. Rev. B: Condens. Matter Mater. Phys.*, 1994, **50**, 5941.
12 K. J. Choi, M. Biegalski, Y. L. Li, A. Sharan, J. Schubert, R. Uecker, P. Reiche, Y. B. Chen, X. Q. Pan, V. Gopalan, L.-Q. Chen, D. G. Schlom and C. B. Eom, *Science*, 2004, **430**, 758.
13 H. Zheng, J. Wang, S. E. Lofland, Z. Ma, L. Mohaddes-Ardabili, T. Zhao, L. Salamanca-Riba, S. R. Shinde, S. B. Ogale, F. Bai, D. Viehland, Y. Jia, D. G. Schlom, M. Wuttig, A. Roytburd and R. Ramesh, *Science*, 2004, **303**, 661.
14 S. A. Harrington, J. Zhai, S. Denev, V. Gopalan, H. Wang, Z. Bi, S. A. T. Redfern, S.-H. Baek, C. W. Bark, C.-B. Eom, Q. Jia, M. E. Vickers and J. L. MacManus-Driscoll, *Nat. Nanotechnol.*, 2011, **6**, 491.
15 A. Kursumovic, E. Defay, O. J. Lee, C.-F. Tsai, Z. Bi, H. Wang and J. L. MacManus-Driscoll, *Adv. Funct. Mater.*, 2013, **23**, 5881.
16 F. Khatkhatay, A. Chen, J. H. Lee, W. Zhang, H. Abdel-Raziq and H. Wang, *ACS Appl. Mater. Interfaces*, 2013, **5**, 12541.
17 A. Dasgupta, S. Saremi, R. Xu, L. Dedon, S. Pandya, A. P. Damodaran and L. W. Martin, *J. Mater. Chem. C*, 2018, **6**, 10751.
18 J. Chang, Y.-S. Park and S.-K. Kim, *Appl. Phys. Lett.*, 2008, **92**, 152910.
19 J. Chakhalian, A. J. Milli and J. Rondinelli, *Nat. Mater.*, 2012, **11**, 92.

20 T. H. Kim, D. Puggioni, Y. Yuan, L. Xie, H. Zhou, N. Campbell, P. J. Ryan, Y. Choi, J. W. Kim, J. R. Patzner, S. Ryu, J. P. Podkaminer, J. Irwin, Y. Ma, C. J. Fennie, M. S. Rzchowski, X. Q. Pan, V. Gopalan, J. Rondinelli and C.-B. Eom, *Nature*, 2016, **533**, 68.
21 M. Gibert, P. Zubko, R. Scherwitzl, J. Íñiguez and J.-M. Triscone, *Nat. Mater.*, 2012, **11**, 195.
22 D. Xiao, W. Zhu, Y. Ran, N. Nagaosa and S. Okamoto, *Nat. Commun.*, 2011, **2**, 596.
23 R. Oja, K. Johnston, J. Frantti and R. M. Nieminen, *Phys. Rev. B: Condens. Matter Mater. Phys.*, 2008, **78**, 094102.
24 H. Wu, X. Ma, Z. Zhang, J. Zeng, J. Wang and G. Chai, *AIP Adv.*, 2016, **6**, 015309.
25 T. Angsten, L. W. Martin and M. Asta, *Phys. Rev. B*, 2017, **95**, 174110.
26 S. Tinte, K. M. Rabe and D. Vanderbilt, *Phys. Rev. B: Condens. Matter Mater. Phys.*, 2003, **68**, 144105.
27 J. Wang, B. W. Eerd, T. Sluka, C. Sandu, M. Cantoni, X.-K. Wei, A. Kvasov, L. McGilly, P. Gemeiner, B. Dkhil, A. Tagantsev, J. Trodahl and N. Setter, *Nat. Mater.*, 2015, **14**, 985.
28 A. Kvasov, L. McGilly, J. Wang, Z. Shi, C. Sandu, T. Sluka, A. Tagantsev and N. Setter, *Nat. Commun.*, 2016, **7**, 12136.
29 V. Moshnyaga, B. Damaschke, O. Shapoval, A. Belenchuk, J. Faupel, O. Lebedev, J. Verbeeck, G. Tendeloo, M. Mücksch, V. Tsurkan, R. Tidecks and K. Samwer, *Nat. Mater.*, 2003, **2**, 247.
30 J. L. MacManus-Driscoll, P. Zerrer, H. Wang, H. Yang, J. Yoon, A. Fouchet, R. Yu, M. Blamire and Q. Jia, *Nat. Mater.*, 2008, **7**, 314.
31 R. Zhao, W.-W. Li, J. Lee, E.-M. Choi, Y. Liang, W. Zhang, R. Tang, H. Wang, Q. Jia, J. L. MacManus-Driscoll and H. Yang, *Adv. Funct. Mater.*, 2014, **24**, 5240.
32 W.-W. Li, R. Zhao, R. Tang, A. Chen, W. Zhang, X. Lu, H. Wang and H. Yang, *ACS Appl. Mater. Interfaces*, 2014, **6**, 5356.
33 W.-W. Li, L. Wang, R. Zhao, R. Tang, Y. Liang and H. Yang, *J. Appl. Phys.*, 2014, **116**, 183904.
34 P. Du, L. Luo, W.-P. Li and Q.-Y. Yue, *J. Appl. Phys.*, 2014, **116**, 014102.
35 F. Li, M. J. Cabral, B. Xu, Z.-X. Cheng, E. C. Dickey, J. M. LeBeau, J.-L. Wang, J. Luo, S. Taylor, W. Hackenberger, L. Bellaiche, Z. Xu, L.-Q. Chen, T. R. Shrout and S.-J. Zhang, *Science*, 2019, **364**, 264.
36 R. G. Munro, Elastic Moduli Data for Polycsystalline Ceramics 6853 (NISTIR, 2002).
37 IEEE, Proceedings of the 5th International Symposium on Micro Machine and Human Science 75, Nagoya, 1994.
38 G. H. Kwei, A. C. Lawson, S. J. L. Billinge and S.-W. Cheong, *J. Phys. Chem.*, 1993, **97**, 2368.
39 A. S. Everhardt, S. Matzen, N. Domingo, G. Ctalan and B. Noheda, *Adv. Electron. Mater.*, 2016, **2**, 1500214.
40 T. Shimizu, D. Suwama, H. Taniguchi, T. Taniyama and M. Itoh, *J. Phys.: Condens. Matter*, 2013, **25**, 132001.
41 Y. Shintani and O. Tada, *J. Appl. Phys.*, 1970, **41**, 2376.
42 K. Iijima, T. Terashima, K. Yamamoto, K. Hirata and Y. Bando, *Appl. Phys. Lett.*, 1990, **56**, 527.
43 K. Abe, S. Konatsu, N. Yanase, K. Sano and T. Kawakubo, *Jpn. J. Appl. Phys.*, 1997, **36**, 5846.
44 B. Noheda, J. A. Gonzalo, L. E. Cross, R. Guo, S.-E. Park, D. E. Cox and G. Shirane, *Phys. Rev. B: Condens. Matter Mater. Phys.*, 2000, **61**, 8687.
45 L. Bellaiche, A. Garcia and D. Vanderbilt, *Phys. Rev. Lett.*, 2000, **84**, 5427.
46 Y. M. Jin, Y. Wang, A. G. Khachaturyan, J. F. Li and D. Viehland, *Phys. Rev. Lett.*, 2003, **91**, 197601.
47 K. Yao, H. Kakemoto, T. Tsurumi and S. Wada, *Mater. Sci. Eng., B*, 2005, **120**, 181.
48 Z. H. Zhou, X. S. Gao, J. Wang, K. Fujihara, S. Ramakrishna and V. Nagarajan, *Appl. Phys. Lett.*, 2007, **90**, 052902.
49 V. Nagarajan, A. Roytburd, A. Stanishevsky, S. Prasertchoung, T. Zhao, L. Chen, J. Melngailis, O. Auciello and R. Ramesh, *Nat. Mater.*, 2003, **2**, 43–47.
50 A. G. Agronin, Y. Rosenwaks and G. I. Rosenman, *Nano Lett.*, 2003, **3**, 169–171.
51 A. Labuda and R. Proksch, *Appl. Phys. Lett.*, 2015, **106**, 253103.
52 T. Jungk, Á. Hoffmann and E. Soergel, *Appl. Phys. Lett.*, 2007, **91**, 253511.
53 B. Y. Huang, E. N. Esfahani and J. Y. Li, *Natl. Sci. Rev.*, 2019, **6**, 55–63.
54 Q. F. Zhu, E. N. Esfahani, S. H. Xie and J. Y. Li, *Theor. Appl. Mech. Lett.*, 2020, **10**, 23–26.
55 T. Jungk, Á. Hoffmann and E. Soergel, *Appl. Phys. Lett.*, 2006, **89**, 163507.
56 A. Gannepalli, D. G. Yablon, A. H. Tsou and R. Proksch, *Nanotechnology*, 2013, **24**, 355705.
57 I.-D. Kim, Y. Avrahami, H. L. Tuller, Y.-B. Park, M. J. Dicken and H. A. Atwater, *Appl. Phys. Lett.*, 2005, **86**, 192907.
58 B. C. Luo, D. Y. Wang, M. M. Duan and S. Li, *Appl. Phys. Lett.*, 2013, **103**, 122903.
59 A. Piorra, A. Petraru, H. Kohlstedt, M. Wuttig and E. Quandt, *J. Appl. Phys.*, 2011, **109**, 104101.
60 Z. Wang, L. Yan, Y. Yang, J. Li, J. Das, A. L. Geiler, A. Yang, Y. Chen, V. G. Harris and D. Viehland, *J. Appl. Phys.*, 2011, **109**, 034102.
61 C. Deng, Y. Zhang, J. Ma, Y. Lin and C.-W. Nan, *Acta Mater.*, 2008, **56**, 405.
62 A. Raeliarijaona and H. Fu, *J. Appl. Phys.*, 2014, **115**, 054105.